Monthly Notices
of the
ROYAL ASTRONOMICAL SOCIETY

MNRAS **516,** 2641–2652 (2022) https://doi.org/10.1093/mnras/stac2392
Advance Access publication 2022 August 26

MeerKAT radio observations of the neutron star low-mass X-ray binary Cen X–4 at low accretion rates

J. van den Eijnden,[1★] R. Fender,[1,2] J. C. A. Miller-Jones,[3] T. D. Russell,[4] P. Saikia,[5] G. R. Sivakoff[6] and F. Carotenuto[1]

[1] *Department of Physics, Astrophysics, University of Oxford, Denys Wilkinson Building, Keble Road, Oxford OX1 3RH, UK*
[2] *Department of Astronomy, University of Cape Town, Private Bag X3, Rondebosch 7701, South Africa*
[3] *International Centre for Radio Astronomy Research, Curtin University, GPO Box U1987, Perth, WA 6845, Australia*
[4] *INAF, Istituto di Astrofisica Spaziale e Fisica Cosmica, Via U. La Malfa 153, I-90146 Palermo, Italy*
[5] *Center for Astro, Particle and Planetary Physics (CAP^3), New York University Abu Dhabi, PO Box 129188 Abu Dhabi, UAE*
[6] *Department of Physics, CCIS 4-181, University of Alberta, Edmonton, AB T6G 2E1, Canada*

Accepted 2022 August 22. Received 2022 August 22; in original form 2022 July 8

ABSTRACT

Centaurus X–4 (Cen X–4) is a relatively nearby neutron star low-mass X-ray binary that showed outbursts in 1969 and 1979, but has not shown a full outburst since. Due to its proximity and sustained period of quiescence, it is a prime target to study the coupling between accretion and jet ejection in quiescent neutron star low-mass X-ray binaries. Here, we present four MeerKAT radio observations at 1.3 GHz of Cen X–4, combined with *NICER* and *Swift* X-ray monitoring. During the first and most sensitive observation, Cen X–4 was in a fully quiescent X-ray state. The three later and shorter observations targeted a brief period of faint X-ray activity in 2021 January, which has been referred to as a 'mis-fired' outburst. Cen X–4 is not detected in any of the four MeerKAT observations. We place these radio non-detections on the X-ray–radio luminosity diagram, improving the constraints on the correlation between the two luminosities from earlier quiescent radio studies. We confirm that Cen X–4 is radio fainter than the transitional millisecond pulsar PSR J1023+0038 at the same X-ray luminosity. We discuss the radio behaviour of accreting neutron stars at low X-ray luminosity more generally and finally comment on future observing campaigns.

Key words: accretion, accretion discs – stars: neutron – X-rays: binaries.

1 INTRODUCTION

Low-mass X-ray binaries (LMXBs), wherein a black hole (BH) or neutron star (NS) accretes from a binary companion star, are routinely used to study the connection between accretion and the launch of outflows. Such outflows can take two forms, namely highly collimated and often relativistic outflows from the inner accretion flow called jets, and slower, more massive disc winds with a wider opening angle and a range of launch radii. A large fraction of LMXBs are transient sources, spending most of their lifetimes in quiescent states where little to no accretion takes place. Intermittently, these transient LMXBs show outbursts, where the accretion disc transitions into a hot, ionized state, and the accretion rate increases by orders of magnitude. Alternatively, persistently accreting LMXBs do not show outburst-quiescence cycles, and their accretion disc instead remains in the ionized outburst state (see e.g. Done, Gierlinski & Kubota 2007; Gilfanov 2010, for reviews).

LMXBs in outburst can reside in different spectral-timing states (Fender, Belloni & Gallo 2004): the system rises in accretion rate in the hard state, where its X-ray emission is highly variable and dominated by the Comptonized emission from an optically thin population of hot electrons often called the corona. Via intermediate spectral-timing states, it then often transitions into the soft state, characterized by weak X-ray variability and emission from an optically thick, geometrically thin disc. While it may transition to a high Eddington accretion state or make multiple transitions between the hard and soft state, during the outburst decay, it transitions from the soft into the hard state at lower X-ray luminosities than the hard-to-soft transition (Maccarone & Coppi 2003). Finally the outburst sinks back into quiescence. The spectral-timing states of NSs are historically named differently, with the main classification into atoll and Z-sources based on the shape of the tracks they display in their X-ray colour–colour diagrams. Within both the atoll and Z-classifications, several sub-states have been identified (see e.g. Hasinger & van der Klis 1989; Van der Klis 2006, for details). The discovery of an NS LMXBs transitioning between the atoll and Z-source classifications showed that mass-accretion rate fundamentally underlies the difference between the classes, with the latter at the highest accretion rates (Homan et al. 2007). Despite these different historical spectral-timing classifications between NS and BH systems, several authors have identified equivalencies between the states across both source types (e.g. Migliari & Fender 2006; Muñoz-Darias et al. 2014).

These LMXB states are intricately linked to their outflow properties. In BH systems, the hard state is associated with the continuous

---

★ E-mail: jakob.vandeneijnden@physics.ox.ac.uk

launch of a compact jet, followed by the launch of discrete ejecta during the hard-to-soft transitional states, while the compact jet in quenched in the soft state (e.g. Fender et al. 2004; Russell et al. 2019b). In atolls, which can (but do not always) change between Comptonization-dominated ('hard', island state) and thermal-dominated ('soft' banana state) states, compact jets are observed routinely in the former (Migliari et al. 2003; Migliari & Fender 2006; Gusinskaia et al. 2020). However, whether jet quenching in the latter state always occurs remains unclear (Rutledge et al. 1998; Migliari et al. 2004; Miller-Jones et al. 2010; Fender 2016; Gusinskaia et al. 2017; van den Eijnden et al. 2021a). The Z-sources show compact jets and discrete ejecta, depending on the exact branch of their Z-track (Migliari & Fender 2006). Disc winds were initially observed in the X-ray band, where they show up in BH soft states and are easiest to observe in high inclination systems (Ponti et al. 2012). However, disc winds are also observed in the optical (e.g. Muñoz-Darias et al. 2016) and IR band (e.g. Sánchez-Sierras & Muñoz-Darias 2020): optical winds are observed in the hard state, while IR winds are seen across the outburst. Recently, the first UV wind detection was reported in an NS LMXB (Castro Segura et al. 2022). Finally, outburst light-curve modelling also suggests strong outflows (Tetarenko et al. 2018).

The connection between the accretion flow and compact jets is routinely studied in the X-ray–radio luminosity (L_X–L_R) diagram. Here, the former traces the accretion luminosity and is a proxy for accretion rate, while the latter traces the jet and its brightness. Compact BH jets show an L_X–L_R correlation across ~eight orders of magnitude in X-ray luminosity (Hannikainen et al. 1998; Corbel et al. 2000, 2003; Gallo et al. 2006); a subset of sources follows a radio-bright correlation with a power-law slope of $\beta \approx 0.6$ (where $L_R \propto L_X^{\beta}$, while others follow a steeper correlation with $\beta \gtrsim 1$ at high X-ray luminosities, before re-joining the other track around $L_X \approx 10^{35}$ erg s^{-1} (e.g. Coriat et al. 2011; Soleri & Fender 2011; Carotenuto et al. 2021, although discussion exists regarding the statistical robustness of this separation; e.g. Gallo, Degenaar & van den Eijnden 2018). The situation for NS LMXBs is even more complex. While, as a sample, NS LMXBs are ~22 times radio-fainter than BH systems, the individual NS systems do not appear to follow a single correlation; significant scatter exists both between sources and between outbursts of the same source. Furthermore, due to their radio faintness, few sources have been monitored over a large range of X-ray luminosity – particularly below $L_X \approx 10^{35}$ erg s^{-1}, few NS LMXBs have been detected in radio (e.g. Tudor et al. 2017; Gusinskaia et al. 2020). For the sample of NS LMXBs, however, a power-law slope of $\beta \approx 0.4$– -0.5 has been measured (Gallo et al. 2018), which is similar to BHs. Different radiative efficiencies may be expected for the two types of LMXBs–BHs can advect a fraction of the liberated gravitational energy across the event horizon, while the presence of an NS surface implies that all this liberated energy should, eventually, be radiated. Therefore, a similarity in the L_X–L_R coupling of the two source classes, which depends on this radiative efficiency, is surprising.

While BH systems have been radio-detected in quiescent states down to $L_X < 10^{31}$ erg s^{-1} (Gallo et al. 2006; Dinçer et al. 2018), no NS LMXB radio detections have been obtained below $L_X = 10^{34}$ erg s^{-1}.[1] Moreover, few radio upper limits exist in this X-ray regime. Therefore, the correlation between the accretion flow and compact jets is poorly known for weakly accreting and quiescent NS LMXBs, and either radio detections or deeper upper limits in this regime are necessary to advance our understanding. In this work, we present a dedicated radio and X-ray campaign of the NS LMXB Centaurus X–4 (Cen X–4) to constrain the low-L_X inflow-outflow coupling.

Table 1. Summary of the MeerKAT radio observations of Cen X–4. The Start MJD column refers to the first on-target scan, and the on-source time does not include setup or calibration scans. The radio luminosity L_R is calculated assuming a distance of 1.2 kpc, and limits are quoted at 3-σ significance.

	Start MJD	On-source time	RMS sensitivity (μJy bm^{-1})	5-GHz L_R (erg s^{-1})
1	59118.54	4 h	4.3	$<1.1 \times 10^{26}$
2	59221.43	15 min	23	$<5.9 \times 10^{26}$
3	59223.36	15 min	18	$<4.7 \times 10^{26}$
4	59230.32	15 min	16	$<4.1 \times 10^{26}$

Cen X–4 is a close-by transient NS LMXB, located at a relatively close-by distance: Chevalier et al. (1989) determine $d = 1.2 \pm 0.3$ kpc, while recent *Gaia* measurements imply a slightly larger distance (see Section 4). It was discovered originally in outburst in 1969 (Conner, Evans & Belian 1969) and showed a second outburst in 1979 (Kaluzienski, Holt & Swank 1980). Observations with the Very Large Array detected its radio counterpart and monitored it during the 1979 outburst (Hjellming 1979; Hjellming et al. 1988). Searches for radio emission during quiescence yielded no detections, despite its small distance (Kulkarni et al. 1992; Tudor et al. 2017). However, the limit found by Tudor et al. (2017) provides the deepest radio constraint on a quiescent NS LMXB and therefore provides the best low-L_X anchor to the NS L_X–L_R relation to date. In 2021 January, long-term optical monitoring of Cen X–4 in the XB-NEWS program (Waterval et al. 2020) revealed the onset of activity in all optical bands (Saikia et al. 2021). X-ray follow up observations confirmed the activity (van den Eijnden et al. 2021b). However, the source did not enter a full outburst phase, but instead returned to quiescent levels at all wavelengths two weeks later (van den Eijnden et al. 2021c). This behaviour has been referred to as a 'mis-fired' outburst, caused either by an inside-out heating front stalled by low levels of irradiation in the outer accretion disc, or by a local thermal-viscous instability in the disc (Baglio et al. 2022). In this paper, we present MeerKAT radio observations of Cen X–4 taken in its quiescent state in 2020 September and during the brief period of activity in 2021 January.

2 OBSERVATIONS AND DATA REDUCTION

2.1 Radio: MeerKAT

We performed a total of four observations of the field surrounding Cen X–4 (J2000 $14^{\mathrm{h}}58^{\mathrm{m}}21.935^{\mathrm{s}}$, $-31^{\circ}40'07.52''$) with MeerKAT. The first observation was taken on 2020 September 26 (capture block 1601122564), while Cen X–4 was in its usual quiescent state, with a longer, 4.5-h observation time including overheads (~4 h on target). The three remaining observations were taken during the brief period of activity in 2021 January, specifically on 2021 January 7, 9, and 16 (capture blocks 1610014143, 1610180483, 1610782322, respectively). Those latter three observations were all shorter, providing 15 min on-target observing time. All observations were taken as part of the ThunderKAT Large Survey Program (Fender et al. 2016), which monitors active transient X-ray binaries on a weekly basis and performs additional dedicated observations of individual X-ray binaries, such as the quiescent observation of Cen X–4. Observational details are also summarized in Table 1.

---

[1] Here, we ignore the transitional millisecond pulsars, which we will discuss in Section 4.

All four observations were performed using the *L*-band receivers, providing an observing band between 856 and 1712 MHz, for a central frequency of 1.3 GHz. The data were collected in 32k-mode (i.e. 32768 frequency channels) and standard integration time of 8 s. The (standard) primary and nearby secondary calibrator sources were J1939-6342 and J1501-3918, respectively. The former was observed at the start of each observation for 5 min. 2-min scans of the latter source bookended the target scan during the three short observations, while such scans were performed every 30 min during the longer 2020 September observation.

We used the OXKAT suite of analysis scripts (Heywood 2020)[2] to perform flagging, calibration, and imaging of the observations. Through OXKAT we used the COMMON ASTRONOMY SOFTWARE APPLICATION (CASA; McMullin et al. 2007) to perform initial data averaging, flagging, and calibration. Afterwards, we applied the bandpass, flux-scale, complex gain, and delay corrections to the target scans, and split of the target data, before flagging and imaging these data using the TRICOLOUR and WSCLEAN (Offringa et al. 2014) packages, respectively. Next, we applied self-calibration and re-imaged the field. Finally (as no source was detected at the position of Cen X-4), we placed upper limits on the flux density at three times the RMS sensitivity over a region covering the source position that was also devoid of detected point sources in the longer observation.

2.2 X-rays: *Swift* and *NICER*

During the time frame of the MeerKAT observations, the *Neil Gehrels Swift Observatory* (hereafter *Swift*) X-ray Telescope (XRT) observed Cen X–4 seventeen times. On 2020 September 26 (ObsID 00088937006), a coordinated observation was performed simultaneously with the deep MeerKAT observation, for a total exposure of ∼3 ks in Photon-Counting (PC) mode. Later, during the brief period of activity around 2021 January, *Swift*/XRT observed a further sixteen times in PC mode between 2020 December 28 and 2021 February 4 with shorter exposures ranging from ∼0.2 to ∼1.0 ks. To monitor the profile of the X-ray activity, we extracted count rates for all observations using the Online Data Products Pipeline (Evans et al. 2007).[3]

To measure the X-ray flux evolution during the observations, we also extracted the X-ray spectrum for each observation. We downloaded the raw data from the HEASARC and used the RUN_XRTPIPE.PL script to perform standard data reduction. We then created source and background regions by defining a circular source region with a 59 arcsec diameter (25 pixels; Evans et al. 2007) centred on the brightest target pixel and an annular background region with inner and outer diameters of 59 and 400 arcsec, respectively. Due to the low flux of Cen X–4 and the short *Swift* exposures, five observations did not detect sufficient counts for a spectral analysis (i.e. between 2 and 17 counts in the source region). Therefore, we only extracted source and background spectra from the remaining twelve observations, using XSELECT. We then created the observation-specific ARF-response files using the XRTMKARF tool and downloaded the appropriate RMF-response file, SWXPC0TO12S6_20130101V014.RMF, from the CALDB. Finally, we rebinned all twelve spectra to at least 1 count per bin using GRPPHA. In all steps we used HEASOFT v6.29. We also used *Swift's* Online Data Products Pipeline to extract the X-ray spectra for the same observations, to re-perform our spectral analysis and confirm that the results are consistent.

Swift/XRT did not observe within 24 h from the 2021 January 9 MeerKAT observation. However, the *Neutron Star Interior ExploreR* (*NICER*) observed with a ∼0.53 ks cumulative[4] exposure on that day (ObsID 3652010901). *NICER* is a single-pixel instrument with a lower angular resolution than *Swift*/XRT (particularly in PC mode), a softer response, and higher background count rate. Therefore, *NICER* spectra should be examined carefully when observing faint sources such as Cen X–4, for instance to determine the energy range where the source dominates over the background. Hence, we only extract the *NICER* spectrum when no *Swift* data areis available. To extract the *NICER* spectrum, we downloaded the HEASARC datafile and ran the NICERL2 tool to re-apply the level-2 calibration using the latest version of the CALDB. We then used XSELECT to extract the target spectrum, without specific energy cuts, as we checked the energy range where the source dominates explicitly before spectral fitting. We then created response files using the NICERRMF and NICERARF tools, before calculating the background spectrum using the NICER_BKG_ESTIMATOR tool.[5] We finally rebinned the spectrum to 20 counts per bin.

All X-ray spectral fits, for both *Swift* and *NICER* observations, were performed in XSPEC v12.12.0 (Arnaud 1996), assuming interstellar abundances from Wilms, Allen & McCray (2000) and cross-sections from Verner et al. (1996). We included the interstellar absorption via the TBABS model and used the convolution model CFLUX whenever we calculated fluxes from the fitted models. We calculated and report all errors at the 1-σ level. Due to the low X-ray count rates, we applied C-statistics (Cash 1979) for all X-ray spectral fitting.

3 RESULTS

3.1 Radio observations

No significant radio emission is detected from the position of Cen X–4 in any of the four MeerKAT observations. In Fig. 1, we show the large-scale field surrounding Cen X–4 (1.4 × 1.4 deg), as observed in the deep, 4.5-h observation. The black cross indicates the position of the X-ray binary. While a large number of unresolved point sources and extended (background) sources are visible in the image, the zoom inset displayed in Fig. 2 (4 × 4 arcmin) confirms that no radio emission associated with Cen X–4 is detected. In the deep, 4.5 h observation, this non-detection implies a 3-σ radio flux density upper limit of 13 μJy at 1.3 GHz, as determined from the image RMS calculated over the target position. In the three shorter observations on 2021 January 7, 9, and 16, the non-detection of Cen X–4 implies 3-σ upper limits of 69, 54, and 48 μJy, respectively. These upper limits are plotted in the bottom panels of the light curves in Fig. 3. For a distance of 1.2 kpc and assuming a flat radio spectrum, these limits correspond to 5-GHz radio luminosity limits of $L_R < 1.1 \times 10^{26}$ erg s^{-1} in the deep observation, and 5.9×10^{26}, 4.7×10^{26}, and 4.1×10^{26} erg s^{-1} in the three shorter observations, respectively.

To test whether short time-scale flaring is present in the observations, we split the three short observations into two equal halves and re-imaged the field. Again, no radio emission is detected in any image at the position of Cen X-4, at RMS sensitivities a factor $\sqrt{2}$ higher than in the full observations. Similarly, we breakup the long

---

[2] https://github.com/IanHeywood/oxkat

[3] https://www.swift.ac.uk/user_objects/

[4] *NICER* ObsIDs typically combine data from multiple exposures on the same day, whose individual durations are short due to the complex visibility of targets as seen from the International Space Station.

[5] See https://heasarc.gsfc.nasa.gov/docs/nicer/tools/nicer_bkg_est_tools.html

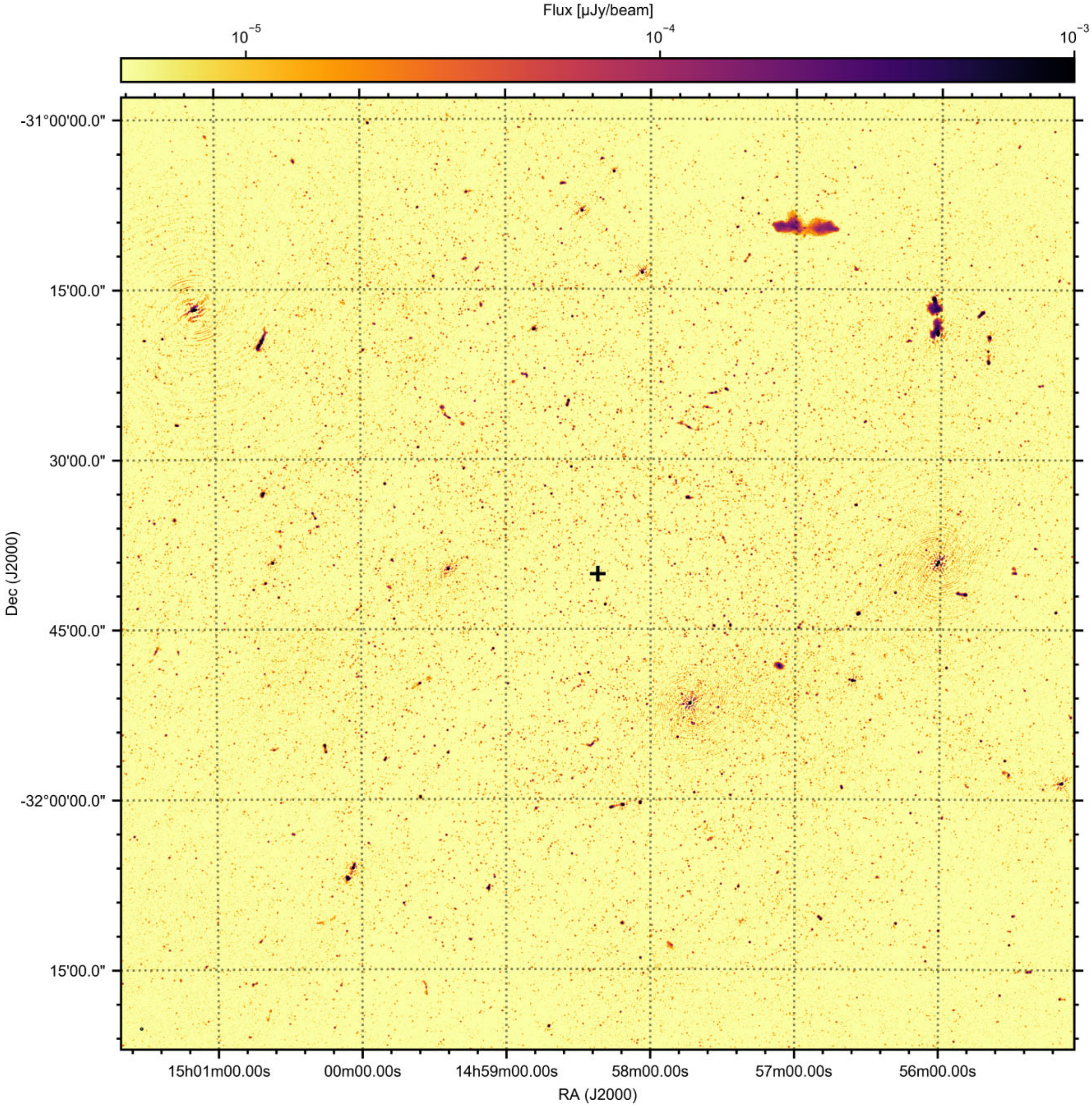

Figure 1. The large-scale 1.3 GHz MeerKAT view of the field surrounding the position of Cen X–4, shown by the black cross. The RMS noise of the image is 4.4 μJy beam^{-1}, obtained in the 4.5-h observation on 2020 September 26. The beam is shown in the lower left-hand corner. A large number of unresolved point sources and extended objects are visible throughout the 1.4 × 1.4 degree field. A zoom around the position of Cen X–4 is shown in Fig. 2, confirming the absence of a MeerKAT radio detection.

quiescent observation into four equal segments lasting two observing scans (∼1 h), optimizing the trade-off between time resolution and sensitivity at these low X-ray luminosities. None of the four radio images show significant emission at the target position, at a sensitivity of 9 μJy bm^{-1}.

3.2 X-ray light curves and spectra

In the top panel of Fig. 3, we plot the *Swift*/XRT light curve around the deep 2020 September radio and X-ray observations (left-hand panel) and during the period of faint activity in 2021 January (right-hand panel). The red dashed lines indicate the times of the four MeerKAT observations. The latter activity shows a rise in X-ray rates over approximately one week, peaking around 0.65 cts s^{-1} in PC mode (see also Saikia et al. 2021; van den Eijnden et al. 2021b). Cen X–4 then decayed over a comparable time-scale (e.g. van den Eijnden et al. 2021c), returning to its typical quiescent count rate levels between ∼10^{-2} and ∼10^{-1} cts s^{-1} (Bernardini et al. 2013).

To calculate the X-ray flux from the *Swift* and *NICER* spectra, we followed the approach of Bernardini et al. (2013), who studied the quiescent *Swift*/XRT PC-mode spectra of Cen X–4 taken daily over a 60-d period. Bernardini et al. (2013) decomposed the spectrum into a soft component emitted by the NS atmosphere and a harder

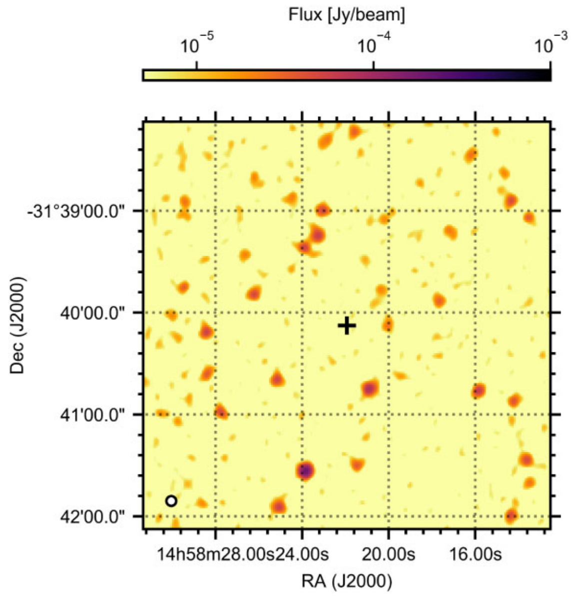

Figure 2. Zoom of the 4 × 4-arcmin field around the position of Cen X–4 in the MeerKAT field shown in Fig. 1. The beam is shown in the bottom left-hand corner. No point source or extended emission is visible at the position of Cen X–4, shown by the black cross, at an RMS sensitivity of 4.4 μJy beam^{-1}.

component attributed to the low-level accretion flow. To perform X-ray modelling at the low cumulative number of counts in the *Swift* spectra, they combined observations in three 0.5–10 keV count-rate ranges to derive typical spectral parameters for the atmosphere and accretion-driven emission: low rates below 7×10^{-2} cts s^{-1}, medium between 7×10^{-2}–1.1×10^{-1} cts s^{-1}, and high above 1.1×10^{-1} cts s^{-1}. As shown by Fig. 3, our observations probe a similar range in X-ray activity of Cen X–4. As we aim to measure the time-dependent flux, we cannot similarly combine observations. However, we can use the template spectra determined in the above three count rate ranges to infer fluxes, when necessary.

Practically speaking, this means we define three ranges for our *Swift* spectra, each with their own approach: (i) for observations exceeding 100 source counts, we directly fit the spectral models to the data; (ii) for observations with <100 counts and a count rate below 7×10^{-2} cts s^{-1}, we fit the overall normalization of the low-rate template spectral model from Bernardini et al. (2013); (iii) for observations with <100 counts and a count rate between 7×10^{-2} and 1.1×10^{-1} cts s^{-1}, we fit the normalization of the medium-rate template spectral model instead. We explain the fits for these three ranges below in more detail. In Table 2, we list the spectral analysis details for each ObsID.

For the three *Swift* spectra with sufficient counts for an actual fit – case (i) – we attempted model fits with three models based on Bernardini et al. (2013): a phenomenological, absorbed power-law model (TBABS∗POWERLAW); a physical, absorbed NS atmosphere model (TBABS∗NSATMOS); and their combination, representing the addition of NS atmospheric and accretion-driven emission (TBABS∗(NSATMOS + POWERLAW)). In all X-ray spectral fits, we fixed the absorption column to $N_H = 8 \times 10^{20}$ cm^{-2}. In all three cases of the high-rate regime, when comparing the single-component models, we find that the power-law model provides a statistically better fit than the NS atmosphere model (i.e. a lower C statistic for the same number of free parameters). The composite model does not provide a statistically better fit in any of the spectra, given the C-statistic improvement for the two extra free parameters. To mirror the approach in cases (ii) and (iii) (see below), we use the 1–10 keV unabsorbed flux from this composite model. However, this flux is consistent with the power-law-only flux in all three cases. All fitted parameters, fit statistics, and fluxes are listed in Table 2. We also confirmed that the fitted parameters and measured fluxes were consistent between the RUN_XRTPIPE.PL and online-pipeline data reduction.

In cases (ii) and (iii), the template model is defined as the third model above, i.e. TBABS∗(NSATMOS + POWER LAW). The difference between the low and medium rate case lies in the parameters of the NS atmosphere and the relative contributions of the two spectral components. In practice, we took the parameters from table 4 in Bernardini et al. (2013), converted the kT^{∞} values to units of Kelvin and the thermal fraction to an NSATMOS normalization, and defined a CONSTANT∗TBABS∗(NSATMOS + POWERLAW) model in XSPEC. We then fitted the constant for each considered spectrum, keeping all other parameters frozen to their template values. Finally, we calculated the X-ray flux by multiplying the 1–10 keV unabsorbed model fluxes of 1.31×10^{-12} erg cm^{-2} s^{-1} (low rates) or 1.60×10^{-12} erg cm^{-2} s^{-1} (medium rates) with the fitted constant. We finally calculated the flux errors by propagating the 1-σ error on the constant to the flux. Our approach implies that we use the full X-ray flux; in the Discussion we will explicitly discuss the contributions of the different spectral components to the flux.

Finally, we turned to the single *NICER* spectrum. Cen X–4 is only detected above the background between 0.5 and 1.5 keV. We assume the medium-rate template spectrum from Bernardini et al. (2013) and again fit the constant scaling factor. This spectral shape gives a significantly better fit than the low-rate template. Moreover, it fits with the rates in the surrounding *Swift* observations, which exceed the maximum rate for the low-rate template.

The light curve of the 1–10 keV unabsorbed X-ray flux is plotted in the middle panels of Fig. 3. The evolution clearly follows the count rate profile, although minor differences are visible. For instance, due to differences in spectral shape, the X-ray flux during the 2020 September observation is significantly lower than that after the return to quiescence in 2021 January, despite both sharing similar count rates. Also, five count-rate data points do not have an associated X-ray flux due to the limited number of source counts. Finally, the *NICER* flux fits well with the general decay trend during that phase of the light curve, despite the small energy range where Cen X–4 is detected.

3.3 The X-ray–radio luminosity plane

To further investigate the low-luminosity inflow/outflow coupling in Cen X–4, we combine X-ray and radio observations and place them on the X-ray–radio luminosity diagram. We match up each radio observation with the X-ray observation taken within 24 h (ObsIDs 00088937006, 00035324071, 3652010901, and 00035324076, chronologically). To convert the X-ray fluxes to 1–10 keV luminosities, we assume a distance of 1.2 kpc (Chevalier et al. 1989, although see Section 4 for a discussion on the distance). To calculate the radio luminosity upper limits from the flux densities, we calculate $L_R = \nu L_\nu$ at a frequency of 5 GHz. This X-ray energy band and radio frequency are chosen to be the same as in the X-ray binary L_X–L_R catalogue by Bahramian & Rushton (2022).

In Fig. 4, we plot the X-ray–radio luminosity diagram for low-mass X-ray binary systems, based largely on Bahramian & Rushton (2022). The green circles show hard-state BH systems, while NSs

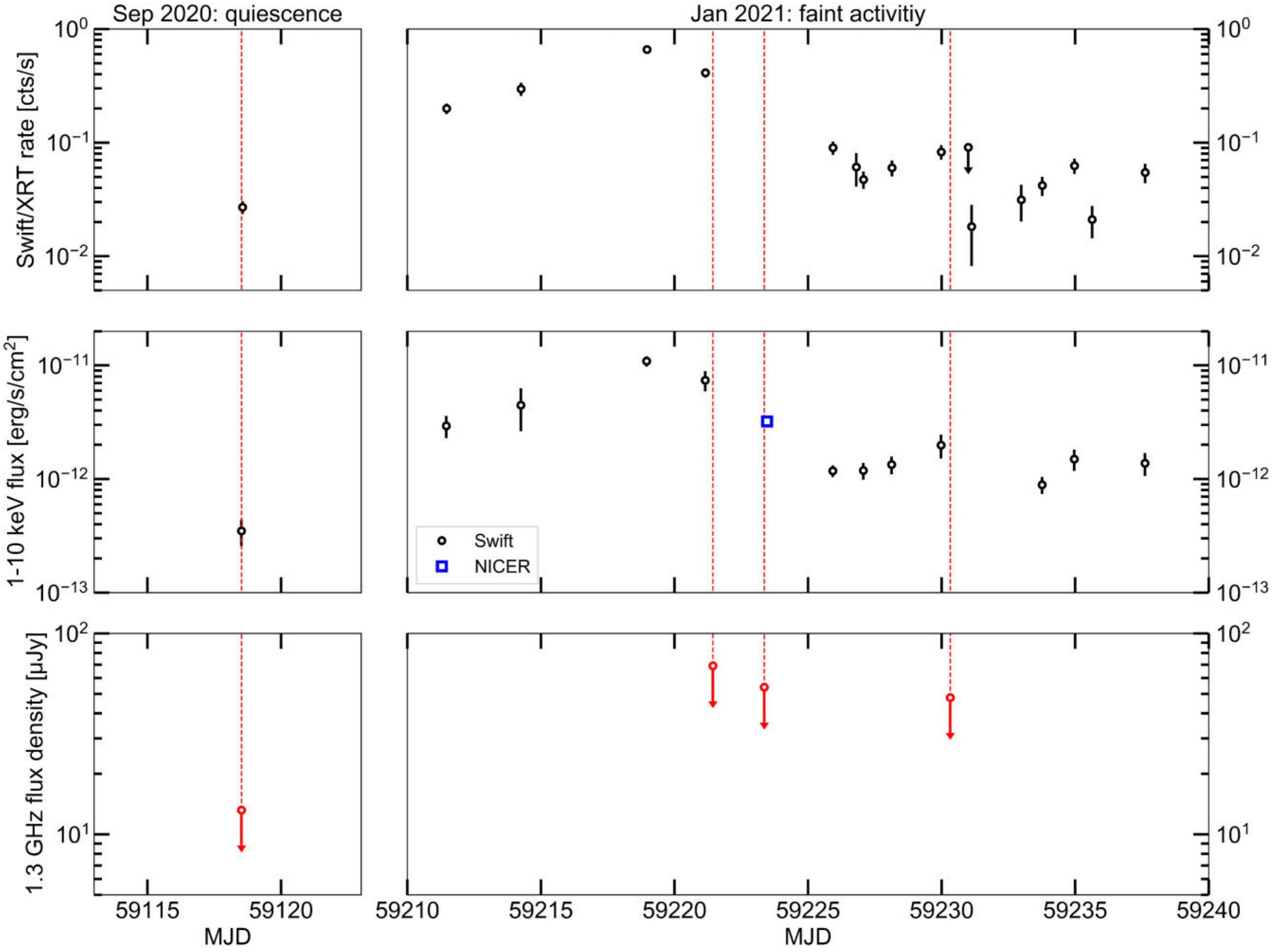

Figure 3. X-ray and radio light curves of Cen X–4 in 2020 September (left-hand panel) and 2021 January (right-hand panel). The top panel shows the *Swift*/XRT count rates, all measured in PC mode. The middle panel shows the 1–10 keV flux measured from the spectral fits to either *Swift* (black circles) or *NICER* (blue square) spectra. The bottom panel shows the radio flux density upper limits for the four MeerKAT observations at 1.3 GHz.

in equivalent states[6] are shown in blue squares. The transitional millisecond pulsars (tMSPs) in their X-ray bright state are shown as the light-green upwards triangles. A number of NS systems are specifically highlighted. Cen X–4 in shown by the stars, where red stars show archival data from Tudor et al. (2017), Hjellming et al. (1988), and Kaluzienski et al. (1980), and turquoise stars show the four observations presented in this work. Aql X-1 is shown with yellow circles, taken from the detailed study by Gusinskaia et al. (2020), which is the most commonly observed system of the NSs plotted here (note that we only plot points where Gusinskaia et al. 2020 calculate a hardness ratio of at least 0.75). Three observations of GRS 1747-312, which we will explicitly discuss in Section 4, are shown by the magenta squares (Panurach et al. 2021). Using distances from Tremou et al. (2018), we also include the quasi-simultaneous data from Panurach et al. (2021) for the globular cluster sources 4U 1746-37, XB 1832-330, X 1850-087, and M15 X-3, which were all observed when actively accreting, although they were relatively X-ray faint.

The deepest MeerKAT radio upper limit of Cen X–4 is comparable to the deep Very Large Array limit obtained by Tudor et al. (2017), but at a ∼4 times higher X-ray luminosity. As a result, the new non-detection reported here is more constraining to the low-luminosity end of the X-ray–radio luminosity correlation for the source. The radio upper limits from the further three MeerKAT observations are at higher luminosities, but as they are taken during the period of faint X-ray activity, they may similarly constrain the slope of this correlation. More generally, radio detections of confirmed NS below $L_X = 10^{34}$ erg s^{-1} are rare. Our observations add four more points to this poorly explored regime, offering a particularly interesting comparison to the tMSPs: this source class has been radio-detected at similar X-ray luminosities, with radio luminosities above or close to the detection threshold of our Cen X–4 observations (see Discussion).

To assess the effect of our new observations on the inferred L_X–L_R coupling, we follow the LINMIX approach, originally developed by Kelly (2007). This MCMC method fits a linear model to data with errors in both the dependent and independent variable, fully accounting for upper limits in the former. It was first applied to the study of the X-ray binary L_X–L_R plane by Gallo et al. (2014), and further adapted by Gusinskaia et al. (2020) and Van den Eijnden et al. (2022) to estimate the uncertainties and account for distance errors. To apply this method, we linearize the correlation model $L_R/L_{R,0} = \xi(L_X/L_{X,0})^\beta$ to

$$\log L_R - \log L_{R,0} = \log \xi + \beta \left(\log L_X - \log L_{X,0}\right) . \qquad (1)$$

---

[6] More specifically, atolls in the island state and the Accreting Millisecond X-ray Pulsars.

Table 2. Details of the X-ray flux determination. For the first three ObsIDs, we list the fitted spectral parameters for the three attempted models: TBABS∗POWERLAW, TBABS∗NSATMOS, and TBABS∗(NSATMOS + POWERLAW), per respective row. For the other ten observations, we instead list the measured *Swift*/XRT PC-mode count rate, the adopted template model shape, and the measured model normalization. For all observations, we list the MJD, C-statistic, number of degrees of freedom (dof), and unabsorbed 1–10 keV X-ray flux. In all fits, we fixed interstellar absorption to $N_H = 8 \times 10^{20}$ cm^{-2}. Due to a low total number of source counts, we did not perform a spectral analysis for *Swift* ObsIDs 00035324073, 00035324077, 00035324078, 00035324079, and 00035324083. All *Swift*/XRT count rates in the top panels of Fig. 3 are available via the link provided in the Data Availability statement. ∗Parameter pegged at lower limit.

Obs	ObsID	MJD	log $T_{\rm eff}$ (K)	$N_{\rm nsa}$	Γ	$N_{\rm po}$ (keV^{-1}cm^{-2}s^{-1})	C (dof)	1–10 keV flux (erg cm^{-2}s^{-1})
Swift	00088937006	59118.52	–	–	3.0 ± 0.3	$(2.3 \pm 0.3) \times 10^{-4}$	40.2 (93)	$(3.3 \pm 0.9) \times 10^{-13}$
			6.3 ± 0.1	$\left(2.1^{+3.4}_{-1.1}\right) \times 10^{-2}$	–	–	49.8 (93)	$(2.8 \pm 0.6) \times 10^{-13}$
			5.0∗	≥0∗	2.8 ± 0.4	$\left(2.1^{+0.4}_{-0.6}\right) \times 10^{-4}$	39.5 (91)	$(3.5 \pm 1.0) \times 10^{-13}$
Swift	00035324070	59218.96	–	–	2.4 ± 0.1	$(4.4 \pm 0.2) \times 10^{-3}$	195.9 (189)	$(1.0 \pm 0.1) \times 10^{-11}$
			>6.47	$\left(5.8^{+3.6}_{-0.4}\right) \times 10^{-2}$	–	–	268.2 (189)	$(8.9 \pm 0.6) \times 10^{-12}$
			$6.25^{+0.11}_{-0.07}$	$\left(3.2^{+3.6}_{-2.6}\right) \times 10^{-1}$	$1.9^{+0.4}_{-0.6}$	$(2.0 \pm 0.1) \times 10^{-3}$	190.6 (187)	$(1.1 \pm 0.1) \times 10^{-11}$
Swift	00035324071	59221.15	–	–	2.7 ± 0.2	$(3.4 \pm 0.3) \times 10^{-3}$	86.0 (89)	$(6.4 \pm 0.9) \times 10^{-12}$
			6.45 ± 0.04	$\left(6.2^{+3.0}_{-2.0}\right) \times 10^{-2}$	–	–	132.3 (89)	$(6.0 \pm 0.7) \times 10^{-12}$
			6.0 ± 0.1	$3.6^{+7.2}_{-2.2}$	1.6 ± 0.6	$\left(9.1^{+1.1}_{-0.6}\right) \times 10^{-4}$	82.3 (87)	$(7.4 \pm 1.5) \times 10^{-12}$
Obs	ObsID	MJD	PC Rate (cts s^{-1})	Template spectrum	Template normalization		C (dof)	1–10 keV flux (erg s^{-1}cm^{-2})
Swift	00035324068	59211.46	1.1×10^{-1}	Medium	1.84 ± 0.22		61.4 (64)	$(2.9 \pm 0.6) \times 10^{-12}$
Swift	00035324069	59214.25	1.1×10^{-1}	Medium	2.79 ± 0.41		42.9 (41)	$(4.5 \pm 1.8) \times 10^{-12}$
NICER	3652010901	59223.46	N/A	Medium	2.07 ± 0.06		102.1 (63)	$(3.2 \pm 0.2) \times 10^{-12}$
Swift	00035324072	59225.93	7.3×10^{-2}	Medium	0.74 ± 0.12		31.0 (35)	$(1.2 \pm 0.1) \times 10^{-12}$
Swift	00035324074	59227.06	4.2×10^{-2}	Low	0.91 ± 0.17		29.4 (30)	$(1.2 \pm 0.1) \times 10^{-12}$
Swift	00035324075	59228.13	5.1×10^{-2}	Low	1.03 ± 0.18		22.4 (35)	$(1.3 \pm 0.2) \times 10^{-12}$
Swift	00035324076	59229.98	6.0×10^{-2}	Low	1.52 ± 0.25		38.5 (34)	$(2.0 \pm 0.5) \times 10^{-12}$
Swift	00035324081	59233.76	3.6×10^{-2}	Low	0.68 ± 0.17		21.0 (22)	$(8.9 \pm 0.2) \times 10^{-13}$
Swift	00035324082	59234.96	4.8×10^{-2}	Low	1.15 ± 0.21		27.2 (34)	$(1.5 \pm 0.3) \times 10^{-12}$
Swift	00035324084	59237.61	3.8×10^{-2}	Low	1.06 ± 0.23		26.0 (23)	$(1.4 \pm 0.3) \times 10^{-12}$

We then apply the PYTHON-implementation of the method[7] to fit the offset and slope of this linear equation, as well as the data's intrinsic scatter, parametrized by a Gaussian standard deviation σ. In particular, we determine for each parameter the median and 16th/84th percentile from 10^4 draws of the posterior distribution. We then follow Gusinskaia et al. (2020) and Van den Eijnden et al. (submitted) and repeat this approach 500 times, each time re-drawing the assumed distance (i.e. scaling the fitted luminosities by a factor $(D_i/D)^2$ for iteration i) from a Gaussian distribution centred at 1.2 kpc with a 0.3 kpc standard deviation. We then determine the fitted parameters and their 1-sigma uncertainties as the mean value of the 500 saved medians and 16th/84th percentiles, respectively.

In Fig. 4, the black line shows the best fit to all Cen X–4 observations, with $\log \xi = -0.14^{+0.22}_{-0.27}$ and $\beta = 0.98^{+0.60}_{-0.28}$. The lightly shaded area indicates the 1-σ confidence interval of the fit.[8] To compare these values to the archival data from Tudor et al. (2017), we exactly repeat these fits without the four MeerKAT data points. In that case, we find $\log \xi_{\rm archival} = -0.12^{+0.23}_{-0.27}$ and $\beta_{\rm archival} = 0.84^{+0.64}_{-0.28}$, which set the 1-$\sigma$ region enclosed by the red dotted lines in Fig. 4. Expectedly, the fitted normalizations are consistent, as these are most strongly constrained by the radio detections during outburst. Similarly, the upper limits on the slope β are almost identical, as these are not affected by the addition of radio upper limits at low L_X. The minimum slope is, on the other hand, more strongly constrained. This can be deduced from comparing the 1-σ regions in Fig. 4 at low L_X. Alternatively, we can compare the 90 per cent lower limit on β from our fit: this limit increases from $\beta \geq 0.51$[9] to $\beta \geq 0.66$ with the addition of the MeerKAT observations.

4 DISCUSSION

In this paper, we have presented four MeerKAT radio observations of the NS LMXB Cen X–4 during quiescence and a period of faint X-ray activity. Cen X–4 is not detected in any of the radio observations, providing deep limits on the correlation between X-ray and radio luminosity in the low-luminosity regime (e.g. $L_X \lesssim 10^{33}$ erg s^{-1}). Here, we will discuss the implication of these measurements for our understanding of (different types of) NSs in the L_X–L_R plane, the origin of the measured X-ray luminosity, and the prospects for low-luminosity NS LMXB radio studies using more sensitive future arrays.

4.1 A note on the distance to Cen X-4

In our analysis, we assumed the 1.2 ± 0.3 kpc distance measured by Chevalier et al. (1989) to convert fluxes and flux densities to luminosities. Recent *Gaia* parallax measurements (Gaia Collaboration 2021), however, imply a slightly larger distance: at 68 per cent

---

[7] Available via https://github.com/jmeyers314/linmix

[8] We note that combining the two X-ray brightest radio epochs, which also returns a non-detection, does not lead to significantly different results of the fit.

[9] This value is consistent with the lower limit reported by Tudor et al. (2017), i.e. $\beta > 0.5$.

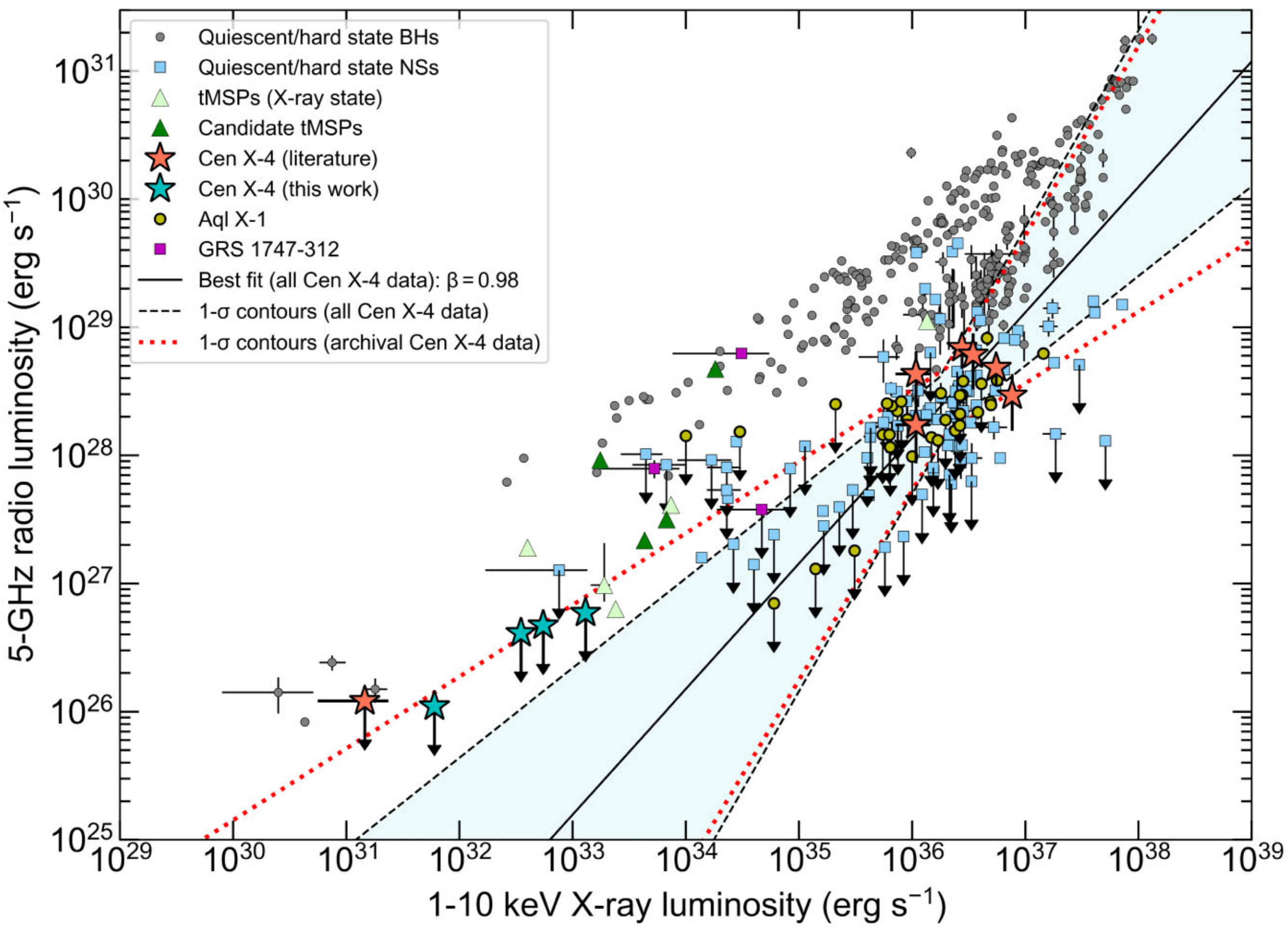

Figure 4. The 1–10 keV X-ray – 5-GHz radio luminosity diagram for low-mass X-ray binaries. The grey circles represent hard-state black hole systems. The light blue squares show neutron stars, particularly hard-state atoll sources and AMXPs. tMSPs are shown as the light green upwards pointing triangles, while four tMSPs are shown as the upwards dark green triangles. We also highlight several sources in particular: Cen X–4 as the stars (red for archival data, turquoise for data from this work), Aql X-1 as the yellow circles, and GRS 1747-312 as the purple squares. For Aql X-1, the compilation of data is taken from Gusinskaia et al. (2020), where we only plot points with an associated hardness ratio exceeding 0.75. The black line indicates the best LINMIX fit to all Cen X–4 data, with the shaded area showing the 1-σ confidence region. The red dotted lines indicate the 1-σ confidence region without the new MeerKAT observations. Plot based on the catalogue by Bahramian & Rushton (2022) with more recent data added (see the text).

confidence, converting the parallax to a distance using the prior for Galactic X-ray binaries from Atri et al. (2019) and applying zero-point corrections, we find $d = 1.87^{+0.75}_{-0.42}$ kpc. To assess the effect of this larger distance on our inferences, we repeat our fits in the L_X–L_R plane after correcting all luminosities by a factor $(1.87/1.2)^2$. This calculation returns consistent parameters: we find $\beta_{\rm gaia} = 0.98^{+0.58}_{-0.28}$ and $\log \xi_{\rm gaia} = -0.13^{+0.23}_{-0.38}$. Finding the same slope is unsurprising, given that both L_X and L_R scale in the same manner with distance. Finding a consistent normalization at $L_{X,0}$ occurs because the best-fitting slope is consistent with linear. Therefore, the main effect of the larger *Gaia* distance is in the comparison with other sources. We will therefore note, in the below discussions, where this may play a role.

4.2 The origin of the X-ray emission

In this work, we have followed the common approach to the X-ray spectra, where the unabsorbed X-ray fluxes from the entire spectral model are calculated to obtain the L_X measurements. However, at the low X-ray luminosities of Cen X–4, the soft X-rays are fitted by an NS atmosphere model, while only the harder X-rays are dominated by the fitted power-law component. When our *Swift* spectra contain enough counts for a model fit, we find that this two-component model does not fit better than a power-law-only model. However, this could likely be caused by the low signal-to-noise, given that analyses by Bernardini et al. (2013) and Chakrabarty et al. (2014) find significant soft thermal emission at similar X-ray luminosity in higher quality spectra. For this reason, and for consistency with the lower quality spectra analysed using two-component template spectral models, we used the two-component X-ray fluxes for all observations.

Since L_X–L_R correlations are interpreted as the observational signature of a coupling between inflow, i.e. mass accretion rate, and outflow, i.e. jet power, we can wonder whether the two-component X-ray flux correctly traces the mass accretion rate. The detailed modelling of the high-energy component by Chakrabarty et al. (2014) is consistent with this component originating in a radiatively inefficient accretion flow, while Bernardini et al. (2013) similarly infer that the power-law-emission seen in *Swift* spectra likely originates from the accretion flow at low mass accretion rate. Moreover, Bernardini et al. (2013) find that the thermal X-rays from the NS atmosphere and the harder X-ray component are variable in a coupled fashion, leading to their conclusion that the full X-ray spectrum is powered by the accretion flow: either directly in the hard component or indirectly, after accreting on to the neutron star surface, in the soft, thermal component. In that interpretation, the combined X-ray luminosity can indeed be used in our L_X–L_R modelling.

For a scenario where all components of the X-ray spectrum are directly or indirectly powered by accretion (instead of e.g. the neutron star surface cooling from previous activity but not actively heated by the instantaneous accretion), the correlation between accretion rate and X-ray luminosity is expected to be linear: as advection of energy across an event horizon is not possible, the process is ultimately expected to be radiatively efficient. In that scenario, although the relative contributions of different spectral components may differ as a function of accretion rate, the correlation between L_X and L_R would remain the same from quiescence to the outburst peak. The lack of radio detections of NS LMXBs below $L_X = 10^{34}$ erg s^{-1} has made it challenging to test this hypothesis; a recent analysis at higher X-ray luminosities for the NS LMXB Aql X-1 by Fijma et al. (2022) did not reveal evidence for any significant effects of the relative contributions of spectral components on the coupling. However, that study also showed how signal-to-noise with current facilities, at distances of several kpc, makes it hard to disentangle such X-ray components, and how the presence of accretion state changes dominates the changes in radio behaviour. Therefore, observations covering quiescence and the rise of the outburst may be most suitable for such a study. However, our MeerKAT results show that current sensitivities in monitoring observations are insufficient for low-L_X radio detections, even at 1.2 kpc.

4.3 NS LMXB jets at low X-ray luminosity

4.3.1 Phenomenological source comparisons

With our radio limits at low X-ray luminosity, we constrain the slope of the L_X–L_R correlation for Cen X–4 to $\beta = 0.98^{+0.59}_{-0.28}$. Using the same fitting approach, Gallo et al. (2018) found a correlation slope of $\beta = 0.44^{+0.05}_{-0.04}$ for the entire sample of NS LMXBs, significantly shallower than our Cen X–4 result. As Cen X–4 is likely an atoll source, a more apt comparison, however, may be with the atoll-only fit performed by Gallo et al. (2018). This atoll-only correlation slope, $\beta = 0.71^{+0.11}_{-0.09}$ is consistent within its 1-σ errors with Cen X–4. As discussed in Gallo et al. (2018), the measured slopes may be affected by the X-ray luminosity distribution of the fitted observations: for the total sample of atolls, which are predominantly observed (and especially radio detected) above 10^{36} erg s^{-1}, this may lead to shallower slopes. With the largest range in X-ray luminosity of any (likely) atoll source, we expect that such issues do not affect our Cen X–4 measurement to the same extent. Recently, Gusinskaia et al. (2020) presented a detailed look at the behaviour of Aql X-1 in the L_X–L_R plane, across various outbursts. When, for the first time, including deep radio limits (i.e. $L_R \lesssim 10^{27}$ erg s^{-1}) between $L_X = 6 \times 10^{34}$ and 3×10^{35} erg s^{-1}, they find a correlation slope of $\beta = 1.17^{+0.30}_{-0.21}$ – again consistent with our Cen X–4 measurement.

Moving beyond comparisons with atoll source, we can turn to other sub-classes of accreting NSs. For instance, our Cen X–4 radio non-detections during its period of faint activity provide stricter confirmation that tMSPs are radio-brighter than other NSs at these low X-ray luminosities (note that the same does not necessarily hold above, e.g. $L_X = 10^{35}$ erg s^{-1}; Russell et al. 2018; van den Eijnden et al. 2018). In particular, the observations of the first-discovered tMSP, PSR J1023+0038, by Deller et al. (2015) lie above our radio upper limits and are excluded from the 1-σ region for Cen X–4's L_X–L_R correlation, for the distance of 1.2 ± 0.3 kpc. This finding confirms the suspicion from Tudor et al. (2017) that observations at higher L_X than theirs, would either detect or disprove the formation of jets in Cen X–4 as radio-bright as tMSPs (although we note that a jet origin for the radio emission of tMSPs is not confirmed; e.g. Bogdanov et al. 2018).

In Fig. 4, we also show four candidate but unconfirmed tMSPs that were recently studied in the L_X–L_R plane as the dark green upward triangles: 3FGL J0427.9-6704 (Li et al. 2020), 3FGL J1544.6-1125 (Jaodand et al. 2021), NGC 6652B (Paduano et al. 2021), and CXOU J110926.4-650224 (Coti Zelati et al. 2021, assuming a 4 kpc distance). We plot one point per source: the radio brightest of four observations for 3FGL J1544.6-1125, and the average X-ray and radio luminosity of the other three. All four are also detected as radio-bright systems, sometimes even consistent with the BH population in the L_X–L_R diagram. Those observations, if the systems are indeed confirmed to be tMSPs, further indicate a clear difference with Cen X–4 at low L_X. If the relative radio brightness of tMSPs is related to interactions between the low-level accretion flow and the pulsar magnetosphere, those interactions should be markedly different than in non-transitioning LMXBs.

Finally, we note that the recent work by Panurach et al. (2021), studying NS LMXBs in globular clusters with the MAVERIC survey, has revealed that low-level-accreting neutron stars can be radio variable. In particular, the transient NS LMXB GRS 1747-312, shown in Fig. 4 as the magenta squares, shows a mixture of radio detections and non-detections, implying radio variability by more than an order of magnitude despite a relatively small range in X-ray luminosity (5×10^{33}–5×10^{34} erg s^{-1}). At a slightly higher $L_X \approx 10^{36}$ erg s^{-1}, Panurach et al. (2021) find that the persistent NS LMXB X 1850-087 is similarly radio variable. In the tMSP population, PSR J1023+0038 also famously shows strong radio variability during its X-ray-bright state: highly structured moding behaviour, anticorrelated with the X-ray band, as well as erratic radio flaring, both on time-scales of minutes (e.g. Bogdanov et al. 2018). During the faint activity period of Cen X-4, we do not find evidence for variability during our observations, when splitting the observing block in two. Longer observations during faint periods of accretion may, in the future, provide better constraints on such variability. Similarly, the longer MeerKAT observation did not reveal evidence for radio variability, during the source's quiescent state.

4.3.2 Correlation breaks and radio-dark propeller outflows

The phenomenological measurements of the L_X–L_R relation discussed in the previous section (i.e. for Aql X-1, all atolls, and ours for Cen X–4), fundamentally assume a single correlation to hold between quiescence and the peak of the outburst (or the state transition where the source may show radio quenching). Gusinskaia et al. (2020) instead also discuss an alternative scenario, where the L_X–L_R correlation of Aql X-1 shows a sharp cutoff a X-ray luminosities below ~5×10^{35} erg s^{-1}.[10] Generally, NS LMXBs appear to change from regular radio detections above $L_X \approx 10^{36}$ erg s^{-1} to mostly radio non-detections at lower X-ray luminosities. While this change is most simplistically explained via a relatively steep, single L_X–L_R correlation, one can explore an explanation for a break in the correlation as well. For Cen X–4 (or any other source,

---

[10] We note that Plotkin et al. (2017) rule out a similar cutoff in the X-ray–radio luminosity relation for the black hole LMXB V404 Cyg. In that work, such a cutoff would be associated with the jet dominating the X-ray emission a low accretion rate.

for that matter), current data do not allow to distinguish between these scenarios: this is particularly difficult due to the ∼3 order of magnitude in X-ray luminosity that has never been covered with radio observations. Similarly, if such a break in the correlation would exist, current data do not constrain whether it occurs at the same X-ray luminosity in different sources.

The X-ray luminosity range where radio non-detections become dominant, is of similar order of magnitude as the range where the onset of the propeller regime is expected. In this regime, the magnetospheric radius, where the NS magnetic field and accretion disc pressure are in balance, moves outside the co-rotation radius due to a decrease in the accretion rate. At the co-rotation radius, the NS spin equals the Keplerian frequency of the disc. Therefore, when the magnetospheric radius moves beyond the co-rotation radius, a centrifugal barrier may be created, halting the accretion flow. The accretion luminosity where this is expected to occur can be written as

$$L_{\rm prop} = 1.6 \times 10^{33}\ B_8^2\ \nu_{100}^{7/3} {\rm erg\ s^{-1}}, \qquad (2)$$

where we assume disc accretion (instead of spherical/wind accretion), B_8 is the magnetic field divided by 10^8 G, and ν_{100} is the spin frequency divided by 100 Hz (Tsygankov et al. 2017). For e.g, Aql X-1, with its 550 Hz spin, $L_{\rm prop}$ can easily match $\sim 5 \times 10^{35}$ erg s^{-1} for a realistic magnetic field of a few times 10^8 G; more generally, for AMXPs with spins at hundreds of Hz, $L_{\rm prop}$ can reasonably be expected to lie between 10^{35} and 10^{36} erg s^{-1}. In the propeller scenario, decaying below $L_{\rm prop}$ would expel material as angular momentum is transferred to the accreting material (Illarionov & Sunyaev 1975). Alternatively, in other models and circumstances, the disc may instead be trapped around the magnetospheric radius, preventing efficient accretion (Spruit & Taam 1993; D'Angelo & Spruit 2010).

The onset of the propeller regime has regularly been suggested to be associated with enhanced radio emission from the outflow. For instance, to explain the difference between the radio luminosity during the decay of outbursts of the AMXP SAX J1808.4-3658, Tudor et al. (2017) invoke a propeller-driven outflow to explain radio detections below $L_X = 10^{36}$ erg s^{-1}. However, one may wonder if additional radio emission, or any radio emission, is always expected in this regime. For instance, if the disc is trapped (mostly expected when L_X drops slightly below $L_{\rm prop}$), it may prevent effective jet launching altogether. Moreover, simulations of the propeller regime by Ustyugova et al. (2006), Romanova et al. (2009), and Lii et al. (2014) show the onset of a two-component outflow: a fast and collimated outflow combined with a more massive, wider-angled and slower wind-like outflow. While radio emission may be expected from the former, it is unclear where the energetic balance between the outflows lies. If most of the energy is carried away by the wind-like slow outflow, which is not expected to emit brightly at radio frequencies, the radio luminosity of NS LMXBs may be suppressed when decreasing below $L_{\rm prop}$.

We reiterate that the onset of such a 'radio-dark' propeller outflow is not necessary to explain current observations; as stated earlier, a relatively steep, single L_X–L_R correlation (per source or the full sample) can similarly account for the currently available data. As discussed below, more sensitive and regular radio monitoring of this low-luminosity regime could provide the data to observationally test the single-correlation hypothesis. However, two brief points are worth stating: first, if a steepening/breaking of the L_X–L_R correlation would be observed in future campaigns, the explanation will likely be related to the NS properties, given the lack of such steepening in black hole systems. Secondly, the idea of the propeller regime suppressing the radio luminosity in an X-ray binary was speculated on earlier by van den Eijnden et al. (2019) for strongly magnetic but slowly spinning accreting NSs (i.e. $B \gtrsim 10^{12}$ G, $\nu < 1$ Hz). In particular, in Swift J0243.6+6124, the archetypal example of a transient, radio-detected X-ray binary in that class, radio emission is observed to turn on and off rapidly across a narrow range in X-ray luminosity. This luminosity could be associated with the propeller transition for reasonable magnetic field strengths for its NS, which are similar to the recent cyclotron line estimates of its magnetic field (Kong et al. 2022).

4.3.3 Observational tests with future observatories

With the planned sensitivity of future arrays, such as the next-generation VLA (ngVLA) or the Square Kilometer Array (SKA, specifically SKA-Mid), we will be able to probe at least an order of magnitude deeper to search for quiescent radio emission from Cen X–4. For instance, the ngVLA's intended 3-σ detection limit at a distance of 1.2 kpc in a short, 15-min observation is 1.2×10^{25} erg s^{-1} (Selina et al. 2018). At these sensitivities, it is possible to directly test for the presence of a break in the L_X–L_R correlation at low X-ray luminosities, and therefore test the idea of dark propeller outflows. If such a correlation break is not observed, it can instead probe the radiative efficiency of the accretion flow down to low accretion rate by measuring or constraining the correlation slope further: a single radio non-detection at $L_X = 10^{32}$ erg s^{-1}, with the 15-min ngVLA sensitivity, would constrain the slope to $\beta \geq 0.8$ (1-σ limit). Taking this further, not detecting Cen X–4 during an exact repeat of our MeerKAT campaign – i.e. at the same X-ray luminosities but with the 15-min ngVLA sensitivity – will imply that $\beta \geq 1.1-1.2$: a limit that starts to constrain the accretion flow to be radiatively efficient (Migliari & Fender 2006).

On a more systematic level, these future radio sensitivity levels could allow for systematic monitoring of quiescent (NS) LMXBs to detect any low-level activity at larger distances than that of Cen X–4. Such systematic programs could (i) detect more examples of low-level activity (i.e. $L_X < 10^{34}$ erg s^{-1}) associated with mis-fired outbursts, and therefore reveal how common such mis-fired outbursts are; (ii) detect the early onset of outbursts to allow for detailed L_X–L_R monitoring; or (iii) provide deep combined images of the quiescent LMXB if no activity is detected. The low-level activity in Cen X–4 was identified by Waterval et al. (2020) due to its small distance in combination with long-term optical monitoring by the XB-NEWS project (Russell et al. 2019a). Currently, no complementary program to XB-NEWS exists at other wavelengths, and the low-level activity falls below the sensitivity of current and planned all-sky X-ray monitors. The ngVLA and SKA-Mid would be suitable for such complementary low-level activity programmes, aimed at the jets instead of the inflow observed in optical: in short, 5-min observations with the ngVLA, one reaches 3-σ detection thresholds of $L_R \approx 2 \times 10^{26}$ erg s^{-1} at 4 kpc. A similar program for BH LMXBs may require even shorter observing times or be possible with sub-arrays to increase observing efficiency: the better established L_X–L_R relation towards quiescence for BHs also removes uncertainty caused by the uncertain nature of this relation at low L_X for NSs.

ACKNOWLEDGEMENTS

The authors thank the anonymous referee for a constructive report. JvdE thanks Joe Bright for discussions on MeerKAT data reduction. JvdE is supported by a Lee Hysan Junior Research Fellowship awarded by St. Hilda's College. We thank the staff at the South African Radio Astronomy Observatory (SARAO) for scheduling these observations. The MeerKAT telescope is operated by the South African Radio Astronomy Observatory, which is a facility of the National Research Foundation, an agency of the Department of Science and Innovation. This work was carried out in part using facilities and data processing pipelines developed at the Inter-University Institute for Data Intensive Astronomy (IDIA). IDIA is a partnership of the Universities of Cape Town, of the Western Cape and of Pretoria. The authors acknowledge the use of public data from the Swift data archive. This research has made use of data and software provided by the High Energy Astrophysics Science Archive Research Center (HEASARC) and NASA's Astrophysics Data System Bibliographic Services. This work has made use of data from the European Space Agency (ESA) mission *Gaia* (https://www.cosmos.esa.int/gaia), processed by the *Gaia* Data Processing and Analysis Consortium (DPAC, https://www.cosmos.esa.int/web/gaia/dpac/consortium). Funding for the DPAC has been provided by national institutions, in particular the institutions participating in the *Gaia* Multilateral Agreement. TDR acknowledges financial contribution from the agreement ASI-INAF n.2017-14-H.0. GRS is supported by NSERC Discovery Grant RGPIN-2021-04001. This work makes use of several python packages, namely NUMPY (Oliphant 2006), ASTROPY (Astropy Collaboration 2013, 2018), MATPLOTLIB (Hunter 2007), and APLPY (Robitaille & Bressert 2012).

DATA AVAILABILITY

A GitHub repository with a JUPYTER notebook and all underlying data to reproduce the figures and analysis in this work will be made public upon acceptance and publication via https://github.com/jvandeneijnden/MeerKATCampaignOfCenXm4.

REFERENCES

Arnaud K. A., 1996, in Jacoby G. H., Barnes J., eds, ASP Conf. Ser. Vol. 101, Astronomical Data Analysis Software and Systems V. Astron. Soc. Pac., San Francisco, p. 17
Astropy Collaboration 2013, A&A, 558, A33
Astropy Collaboration 2018, AJ, 156, 123
Atri P. et al., 2019, MNRAS, 489, 3116
Baglio M. C. et al., 2022, ApJ, 930, 20
Bahramian A., Rushton A., 2022, bersavosh/XRB-LrLx_pub: update 220808
Bernardini F., Cackett E. M., Brown E. F., D'Angelo C., Degenaar N., Miller J. M., Reynolds M., Wijnands R., 2013, MNRAS, 436, 2465
Bogdanov S. et al., 2018, ApJ, 856, 54
Carotenuto F. et al., 2021, MNRAS, 505, L58
Cash W., 1979, ApJ, 228, 939
Castro Segura N. et al., 2022, Nature, 603, 52
Chakrabarty D. et al., 2014, ApJ, 797, 92
Chevalier C., Ilovaisky S. A., van Paradijs J., Pedersen H., van der Klis M., 1989, A&A, 210, 114
Conner J. P., Evans W. D., Belian R. D., 1969, ApJ, 157, L157
Corbel S., Fender R. P., Tzioumis A. K., Nowak M., McIntyre V., Durouchoux P., Sood R., 2000, A&A, 359, 251
Corbel S., Nowak M. A., Fender R. P., Tzioumis A. K., Markoff S., 2003, A&A, 400, 1007
Coriat M. et al., 2011, MNRAS, 414, 677
Coti Zelati F. et al., 2021, A&A, 655, A52
D'Angelo C. R., Spruit H. C., 2010, MNRAS, 406, 1208
Deller A. T. et al., 2015, ApJ, 809, 13
Dinçer T., Bailyn C. D., Miller-Jones J. C. A., Buxton M., MacDonald R. K. D., 2018, ApJ, 852, 4
Done C., Gierlinski M., Kubota A., 2007, A&ARv, 15, 1
Evans P. A. et al., 2007, A&A, 469, 379
Fender R. et al., 2016, in MeerKAT Science: On the Pathway to the SKA. p. 13, preprint (arXiv:1711.04132)
Fender R. P., Belloni T. M., Gallo E., 2004, MNRAS, 355, 1105
Fender R., 2016, Astron. Nachr., 337, 381
Fijma S., van den Eijnden J., Degenaar N., Russell T. D., Miller-Jones J. C. A., 2022, preprint (arXiv:2204.10910)
Gaia Collaboration 2021, A&A, 649, A1
Gallo E. et al., 2014, MNRAS, 445, 290
Gallo E., Degenaar N., van den Eijnden J., 2018, MNRAS, 478, L132
Gallo E., Fender R. P., Miller-Jones J. C. A., Merloni A., Jonker P. G., Heinz S., Maccarone T. J., van der Klis M., 2006, MNRAS, 370, 1351
Gilfanov M., 2010, in Belloni T., ed., Lecture Notes in Physics, Vol. 794, The Jet Paradigm . Springer Verlag, Berlin, p. 17
Gusinskaia N. V. et al., 2017, MNRAS, 470, 1871
Gusinskaia N. V. et al., 2020, MNRAS, 492, 2858
Hannikainen D. C., Hunstead R. W., Campbell-Wilson D., Sood R. K., 1998, A&A, 337, 460
Hasinger G., van der Klis M., 1989, A&A, 225, 79
Heywood I., 2020, oxkat: Semi-automated Imaging of MeerKAT Observations, Astrophysics Source Code Library, record ascl:2009.003
Hjellming R. M., 1979, IAU Circ., 3369, 1
Hjellming R. M., Calovini T. A., Han X. H., Cordova F. A., 1988, ApJ, 335, L75
Homan J. et al., 2007, ApJ, 656, 420
Hunter J. D., 2007, Comput. Sci. Eng., 9, 90
Illarionov A. F., Sunyaev R. A., 1975, A&A, 39, 185
Jaodand A. D. et al., 2021, ApJ, 923, 3
Kaluzienski L. J., Holt S. S., Swank J. H., 1980, ApJ, 241, 779
Kelly B. C., 2007, ApJ, 665, 1489
Kong L.-D. et al., 2022, ApJL, 933, L3
Kulkarni S. R., Navarro J., Vasisht G., Tanaka Y., Nagase F., 1992, in van den Heuvel E. P. J., Rappaport S. A., eds, NATO Advanced Study Institute (ASI) Series C Vol. 377, X-Ray Binaries and Recycled Pulsars. Springer, Berlin, p. 99
Li K.-L., Strader J., Miller-Jones J. C. A., Heinke C. O., Chomiuk L., 2020, ApJ, 895, 89
Lii P. S., Romanova M. M., Ustyugova G. V., Koldoba A. V., Lovelace R. V. E., 2014, MNRAS, 441, 86
Maccarone T. J., Coppi P. S., 2003, MNRAS, 338, 189
McMullin J. P., Waters B., Schiebel D., Young W., Golap K., 2007, in Shaw R. A., Hill F., Bell D. J., eds, ASP Conf. Ser. Vol. 376, Astronomical Data Analysis Software and Systems XVI. Astron. Soc. Pac., San Francisco, p. 127
Migliari S., Fender R. P., 2006, MNRAS, 366, 79
Migliari S., Fender R. P., Rupen M., Jonker P. G., Klein-Wolt M., Hjellming R. M., van der Klis M., 2003, MNRAS, 342, L67
Migliari S., Fender R. P., Rupen M., Wachter S., Jonker P. G., Homan J., van der Klis M., 2004, MNRAS, 351, 186
Miller-Jones J. C. A. et al., 2010, ApJ, 716, L109
Muñoz-Darias T. et al., 2016, Nature, 534, 75
Muñoz-Darias T., Fender R. P., Motta S. E., Belloni T. M., 2014, MNRAS, 443, 3270
Offringa A. R. et al., 2014, MNRAS, 444, 606
Oliphant T. E., 2006, A Guide to NumPy. Trelgol Publishing, p. 85
Paduano A. et al., 2021, MNRAS, 506, 4107
Panurach T. et al., 2021, ApJ, 923, 88
Plotkin R. M. et al., 2017, ApJ, 834, 104
Ponti G., Fender R. P., Begelman M. C., Dunn R. J. H., Neilsen J., Coriat M., 2012, MNRAS, 422, L11
Robitaille T., Bressert E., 2012, APLpy: Astronomical Plotting Library in Python, record ascl:1208.017
Romanova M. M., Ustyugova G. V., Koldoba A. V., Lovelace R. V. E., 2009, MNRAS, 399, 1802
Russell D. M. et al., 2019a, Astron. Nachr., 340, 278

Russell T. D. et al., 2019b, ApJ, 883, 198

Russell T. D., Degenaar N., Wijnands R., van den Eijnden J., Gusinskaia N. V., Hessels J. W. T., Miller-Jones J. C. A., 2018, ApJ, 869, L16

Rutledge R., Moore C., Fox D., Lewin W., van Paradijs J., 1998, Astron. Telegram, 8, 1

Saikia P., Baglio M. C., Russell D. M., Homan J., Waterval S., Bramich D. M., Lewis F., Eijnden J. v. d., 2021, Astron. Telegram, 14302, 1

Sánchez-Sierras J., Muñoz-Darias T., 2020, A&A, 640, L3

Selina R. J. et al., 2018, in Murphy E. J., ed., The ngVLA Reference Design. Astron. Soc. Pac., San Francisco, p. 15

Soleri P., Fender R., 2011, MNRAS, 413, 2269

Spruit H. C., Taam R. E., 1993, ApJ, 402, 593

Tetarenko B. E., Lasota J.-P., Heinke C. O., Dubus G., Sivakoff G. R., 2018, Nature, 554, 69

Tremou E. et al., 2018, ApJ, 862, 16

Tsygankov S. S., Mushtukov A. A., Suleimanov V. F., Doroshenko V., Abolmasov P. K., Lutovinov A. A., Poutanen J., 2017, A&A, 608, A17

Tudor V. et al., 2017, MNRAS, 470, 324

Ustyugova G. V., Koldoba A. V., Romanova M. M., Lovelace R. V. E., 2006, ApJ, 646, 304

van den Eijnden J. et al., 2018, Astron. Telegram, 11520, 1

van den Eijnden J. et al., 2021a, MNRAS, 507, 3899

van den Eijnden J. et al., 2021b, Astron. Telegram, 14303, 1

van den Eijnden J. et al., 2021c, Astron. Telegram, 14317, 1

van den Eijnden J., Degenaar N., Russell T. D., Hernández Santisteban J. V., Wijnands R., Miller-Jones J. C. A., Rouco Escorial A., Sivakoff G. R., 2019, MNRAS, 483, 4628

Van den Eijnden J. et al. 2022, preprint (arXiv:2208.14903)

Van der Klis M., 2006, in Lewin W., Van der Klis M., eds, Compact Stellar X-ray Sources. Cambridge Univ. Press, Cambridge, p. 39

Verner D. A., Ferland G. J., Korista K. T., Yakovlev D. G., 1996, ApJ, 465, 487

Waterval S., Russell D. M., Baglio M. C., Saikia P., Bramich D. M., Homan J., Lewis F., 2020, Astron. Telegram, 14254, 1

Wilms J., Allen A., McCray R., 2000, ApJ, 542, 914

This paper has been typeset from a TEX/LATEX file prepared by the author.